Euro. Jnl of Applied Mathematics (2004), *vol.* 15, *pp.* 625–642.
doi:10.1017/S0956792504005741 Printed in the United Kingdom

Comparison of two dynamic contact line models for driven thin liquid films

RACHEL LEVY and MICHAEL SHEARER

Department of Mathematics and Center for Research in Scientific Computation, North Carolina State University. Raleigh, NC 27695, USA
email: shearer@math.ncsu.edu

(*Received 27 November 2003; revised 29 April 2004*)

The modeling of the motion of a contact line, the triple point at which solid, liquid and air meet, is a major outstanding problem in the fluid mechanics of thin films [2, 9]. In this paper, we compare two well-known models in the specific context of Marangoni driven films. The *precursor model* replaces the contact line by a sharp transition between the bulk fluid and a thin layer of fluid, effectively pre-wetting the solid; the *Navier slip model* replaces the usual no-slip boundary condition by a singular slip condition that is effective only very near the contact line. We restrict attention to traveling wave solutions of the thin film PDE for a film driven up an inclined planar solid surface by a thermally induced surface tension gradient. This involves analyzing third order ODE that depend on several parameters. The two models considered here have subtle differences in their description, requiring a careful treatment when comparing traveling waves and effective contact angles. Numerical results exhibit broad agreement between the two models, but the closest comparison can be done only for a rather restricted range of parameters. The driven film context gives contact angle results quite different from the case of a film moving under the action of gravity alone. The numerical technique for exploring phase portraits for the third order ODE is also used to tabulate the kinetic relation and nucleation condition, information that can be used with the underlying hyperbolic conservation law to explain the rich combination of wave structures observed in simulations of the PDE and in experiments [3, 15].

1 Introduction

In attempting to resolve the well-known stress singularity [8] at a moving contact line, the leading edge of a liquid spreading over a dry solid surface, two strategies are often proposed. One strategy is to introduce a very thin precursor layer of fluid, which is assumed to move hydrodynamically with the bulk fluid behind the contact line. In such a *precursor model*, the contact slope can be associated with the steepest part of the free boundary, i.e., the liquid-air interface, which of course does not come into contact with the solid surface. In the second type of model, the free surface is assumed to achieve contact with the solid surface, but a boundary condition between the fluid and the solid surface permits a small amount of slip of the fluid on the solid, in contrast with the usual no-slip boundary condition. Such a boundary condition was introduced by Navier [19] at the start of a debate concerning suitable liquid-solid boundary conditions [10], leading

eventually to the conclusion that the no-slip boundary condition is realistic for a viscous fluid. The *Navier slip condition* was taken up much later in the context of contact lines [13]; we use the so-called *singular slip* of Greenspan [11] to formulate the Navier slip model.

In this paper, we explore the connections between these two models by doing numerical experiments. Specifically, we simulate traveling wave solutions of equations obtained from the lubrication approximation to the Navier-Stokes equations. We compare contact slopes for the two models, and their dependence upon parameters such as the upstream film height and the precursor height. We restrict attention to a thin film being driven up a solid flat surface by a gradient in surface tension. The surface tension gradient is induced in experiments by a temperature gradient [7, 22], thereby creating a Marangoni surface stress that provides the driving force. In the absence of Marangoni force, a similar study was undertaken by Tuck & Schwartz [20]. In our case, with Marangoni force, we find different behavior, some of which was observed in Buckingham *et al.* [6]. Specifically, preliminary results in Buckingham *et al.* [6] indicated a bounded interval of contact slopes for specific choices of parameters. In this paper, we explore systematically the dependence of the interval of slopes on the parameters.

The thin film, or lubrication, approximation of Stokes flow leads to a single PDE for the height h as a function of position (x, y) on the flat surface, and time t [7]. Neglecting variation in the transverse direction, so that $h = h(x, t)$, the thin film PDE is of the form (cf. Bertozzi *et al.* [3]):

$$h_t + f(h)_x = -(C(h)h_{xxx})_x, \tag{1.1}$$

in which f and C are smooth functions that are positive for $h > 0$; they incorporate effects of gravity, surface tension and the Marangoni force. (We have also dropped second order diffusive terms from (1.1) as they are small [18].) We seek traveling wave solutions, $h(x, t) = \tilde{h}(x - st)$ of (1.1), in which s is the speed of the traveling wave. By substitution into the PDE (1.1) and one integration, we arrive at a third order ODE for $h(\xi)$ (dropping the tilde), where $\xi = x - st$:

$$h''' = \frac{sh - f(h) - sh_m + f(h_m)}{C(h)}, \tag{1.2}$$

in which $' = \frac{d}{d\xi}$, $h_m > 0$ is the upstream height, and s is the wave speed. The computer program we use to understand the structure of solutions of equation (1.2) is modeled on that employed by Buckingham *et al.* [6]. The new code enables us to explore stable and unstable manifolds of the vector field associated with (1.2) with much greater efficiency than earlier procedures, simply by automating much of the selection of parameters. We use the program not only to compare the two models, but also to compute traveling wave information corresponding to a kinetic relation and nucleation condition postulated in LeFloch & Shearer [15] for the underlying scalar conservation law

$$h_t + f(h)_x = 0. \tag{1.3}$$

https://doi.org/10.1017/S0956792504005741 Published online by Cambridge University Press

2 The ODE models

2.1 The Navier Slip model

For the Navier slip model, we adopt the singular slip form of Greenspan [11], which states that at the fluid-solid interface, the fluid velocity u parallel to the interface should be proportional to the strain rate in the fluid, with a coefficient that depends on the height of the film but which blows up at the contact line. Specifically,

$$u = \eta h^{n-2} \frac{\partial u}{\partial z} \quad \text{on } z = 0.$$

Here, $0 < n \leqslant 2$ is an empirical parameter; we take $n = 1$, as suggested in Greenspan [11]; The value $n = 2$ is considered by Hocking [12] and others. The parameter $\eta > 0$ is generally taken to be very small; ηh^{n-2} has the dimension of length; consequently, for $n = 1$, η has the dimension of $(length)^2$; the length scale for the slip is taken to be at least an order of magnitude smaller than the maximum thickness of the film.

The functions C and f of (1.2) take the form (after nondimensionalization as in Bertozzi *et al.* [3]):

$$C(h) = h^3 + \beta h, \quad f(h) = h^2 - h^3 + \frac{2}{3}\beta - \beta h, \tag{2.1}$$

where $\beta > 0$ is a small parameter related to η. Since the fluid surface makes contact with the solid surface, the height becomes zero at some point, which we can take to be the origin. Correspondingly, we impose the boundary conditions

$$h(-\infty) = \lim_{\xi \to -\infty} = h_m, \qquad h(0) = 0$$

on traveling waves. Conservation of mass relates the wave speed s to the upstream height alone, since this speed is also the speed of the contact line, and hence is the (depth averaged) velocity of the fluid parallel to the solid surface:

$$s = \frac{f(h_m)}{h_m}. \tag{2.2}$$

Consequently, the terms $-sh_m + f(h_m)$ in (1.2) are zero for the Navier slip model.

2.2 The precursor model

In the precursor model, we impose the no-slip boundary condition between the fluid and solid surface, corresponding to $\beta = 0$ in (2.1). Thus, the functions in (2.1) simplify to

$$C(h) = h^3, \; f(h) = h^2 - h^3. \tag{2.3}$$

Moreover, the fluid surface does not make contact with the solid surface, so the height remains positive. Correspondingly, we impose boundary conditions

$$h(-\infty) = \lim_{\xi \to -\infty} = h_m, \qquad h(\infty) = \lim_{\xi \to \infty} = h_b,$$

https://doi.org/10.1017/S0956792504005741 Published online by Cambridge University Press

Table 1. *Model specifications*

	Navier Slip	Precursor
Slip parameter	$\beta > 0$	$\beta = 0$
Boundary conditions	$h(-\infty) = h_m$, $h(0) = 0$	$h(-\infty) = h_m$, $h(\infty) = h_b$
Wave speed	$s = \frac{f(h_m)}{h_m}$	$s = \frac{f(h_m)-f(h_b)}{h_m-h_b}$
Flux function	$f(h) = h^2 - h^3 + \frac{2}{3}\beta - \beta h$	$f(h) = h^2 - h^3$

where $h_b < h_m$ is the precursor height. Conservation of mass relates the wave speed s to both the upstream and downstream heights:

$$s = \frac{f(h_m) - f(h_b)}{h_m - h_b}. \tag{2.4}$$

2.3 Comparison

The two models differ in their significant parameters (see Table 1). In the Navier slip model, the parameters are h_m and β, whereas in the precursor model, there are also two parameters, h_m and h_b. However, the boundary condition $h(0) = 0$ from the Navier slip model is at a singular point for the ODE; correspondingly, there is an additional degree of freedom in the ODE solutions for the Navier slip model compared with the precursor model. To compare film profiles for the two models, we later use the technique proposed by Tuck & Schwartz [20], in which a profile with Navier slip corresponds to one with a given precursor height if the maximum heights in the two profiles agree.

2.4 Equilibria

In this section, we consider equation (1.2) as a first order system. Equation (1.2) is

$$h''' = g(h), \qquad \text{where} \qquad g(h) = \frac{sh - f(h) - sh_m + f(h_m)}{h^3 + \beta h}, \tag{2.5}$$

which is equivalent to the first order system

$$\begin{aligned} h' &= u \\ u' &= v \\ v' &= g(h). \end{aligned} \tag{2.6}$$

Equilibria of the system are of the form $(h, u, v) = (\bar{h}, 0, 0)$ with $g(\bar{h}) = 0$, i.e.

$$s(\bar{h} - h_m) = f(\bar{h}) - f(h_m). \tag{2.7}$$

For fixed h_m and s, this equation is represented graphically in Figure 1 as the intersection of a straight line with slope s and the graph of the flux function $f(h)$. For the Navier slip model, the flux function $f(h) = h^2 - h^3 + \frac{2}{3}\beta - \beta h$ intersects the y-axis at $\frac{2}{3}\beta$, and the h axis at $h = 1 - \frac{1}{3}\beta + O(\beta^2)$. Equation (2.2) implies the line with slope s passes through the origin. In the precursor model, the graph of the flux function intersects the origin and the

https://doi.org/10.1017/S0956792504005741 Published online by Cambridge University Press

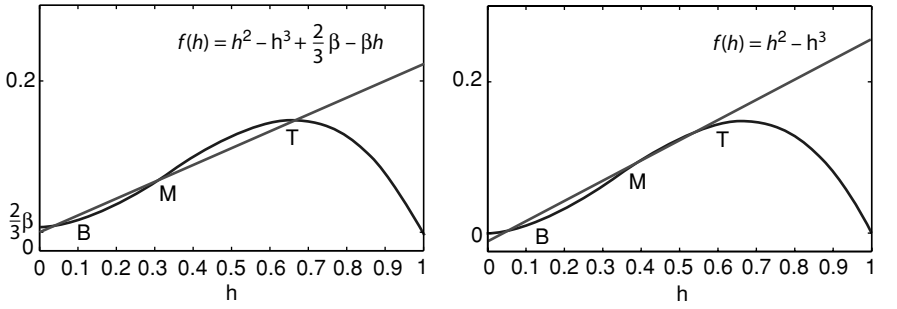

FIGURE 1. Flux functions, line with slope s and equilibria. Navier slip ($\beta = 0.01$ shown); Precursor model ($\beta = 0$).

line with slope s does not, due to (2.4). The line can intersect the flux function as many as three times leading to three equilibria we label from the left B (bottom), M (middle) and T (top).

Let $\bar{h}$ satisfy (2.7). Linearizing (2.5) about $h = \bar{h}$, we obtain

$$w''' = d(\bar{h})w, \quad d(\bar{h}) = \frac{dg}{dh}(\bar{h}).$$

The characteristic equation $\lambda^3 = d(\bar{h})$ has three solutions, a complex conjugate pair $\lambda_{\pm} = \alpha \pm i\gamma$ and a real solution $\lambda_R = (d(\bar{h}))^{\frac{1}{3}}$. The three eigenvalues are spread evenly around the circle with radius $|\lambda_R|$ in the complex plane. Since

$$g'(\bar{h}) = \frac{s - f'(\bar{h})}{\bar{h}^3 + \beta\bar{h}}$$

at an equilibrium, we read off from Figure 1 that $g'(\bar{h}) > 0$ at B and T, while $g'(\bar{h}) < 0$ at M. Consequently, B and T have one-dimensional unstable manifolds $W^U(B)$, $W^U(T)$ and two-dimensional stable manifolds $W^S(B)$, $W^S(T)$. Similarly, M has a two-dimensional unstable manifold $W^U(M)$ and one-dimensional stable manifold $W^S(M)$.

Remark

In the Navier slip model, we consider trajectories that connect to $h = 0$. These are trajectories originating at the middle equilibrium M rather than at B or T; while there may be trajectories from these other equilibria, they are less significant for our purpose, as there are fewer such trajectories: the unstable manifolds from B and T are one-dimensional, whereas the unstable manifold from M is two-dimensional. A consequence is that even for the Navier slip model we consider parameter values for which there are three equilibria.

To capture the two-dimensional invariant manifold of an equilibrium $(\bar{h}, 0, 0)$, we set initial conditions on the tangent plane at $(\bar{h}, 0, 0)$. The tangent plane is generated by solutions of the linear system

$$\hat{h}' = \hat{u}$$
$$\hat{u}' = \hat{v}$$
$$\hat{v}' = d(\bar{h})\hat{h}$$

https://doi.org/10.1017/S0956792504005741 Published online by Cambridge University Press

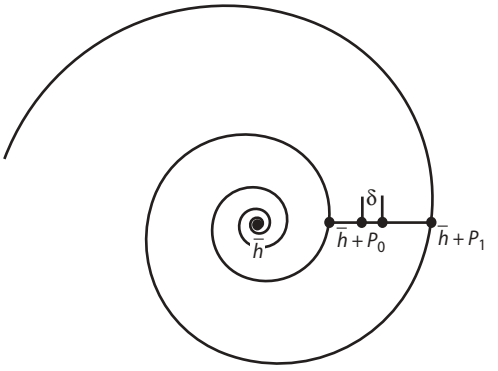

FIGURE 2. Choosing initial data on the invariant manifold.

corresponding to the complex conjugate eigenvalues $\lambda_{\pm} = \alpha \pm i\gamma$. Thus,

$$\begin{pmatrix} \hat{h} \\ \hat{u} \\ \hat{v} \end{pmatrix}(\xi) = ae^{\alpha\xi}(\cos\gamma\xi\,\mathbf{v}_1 - \sin\gamma\xi\,\mathbf{v}_2) \tag{2.8}$$

where

$$\mathbf{v}_1 = \begin{pmatrix} 1 \\ \alpha \\ \alpha^2 - \gamma^2 \end{pmatrix} \quad \text{and} \quad \mathbf{v}_2 = \begin{pmatrix} 0 \\ \alpha \\ 2\alpha\gamma \end{pmatrix}$$

generate the tangent plane.

Consider the unstable case, in which $\alpha > 0$. In choosing initial data for the ODE simulation, we take a radial line in the tangent plane, i.e. a straight line emanating from the equilibrium, and limit initial points to points on the line between successive crossings of a single trajectory spiraling out from or into the equilibrium. From (2.8), successive crossings occur at times differing by $\frac{2\pi}{\gamma}$; correspondingly

$$(\hat{h}, \hat{u}, \hat{v})(\xi + 2\pi/\gamma) = e^{\frac{2\pi\alpha}{\gamma}}(\hat{h}, \hat{u}, \hat{v})(\xi).$$

Thus, if we select one point P_0 in the tangent plane, we capture all trajectories in the two-dimensional manifold by selecting initial data on the line between $(\bar{h}, 0, 0) + P_0$ and $(\bar{h}, 0, 0) + e^{\frac{2\pi\alpha}{\gamma}} P_0$. (See Figure 2, in which the equilibrium is labeled $\bar{h}$, and the two points are labeled $\bar{h} + P_0, \bar{h} + P_1$.) Note that $\gamma/\alpha = \tan\frac{\pi}{3}$, so that $e^{\frac{2\pi\alpha}{\gamma}} \approx 37.6223$. To select P_0, we can choose a and ξ in (2.8). Without loss of generality, we choose $\xi = 0$. However, for accuracy, we need to choose P_0 close to the origin, so $a = a_0$ is chosen to be small.

To summarize, we initiate ODE simulations at $\xi = 0$, with

$$\begin{pmatrix} h \\ u \\ v \end{pmatrix}(0) = \begin{pmatrix} \bar{h} \\ 0 \\ 0 \end{pmatrix} + a \begin{pmatrix} 1 \\ \alpha \\ \alpha^2 - \gamma^2 \end{pmatrix}. \tag{2.9}$$

Here, the parameter a is chosen in an interval $[a_0, a_0 e^{\frac{2\pi\alpha}{\gamma}})$, to capture all trajectories in the two-dimensional invariant manifold. In practice, the choice of a is crucial, and for greater resolution, or to focus on one part of the solution set, we often take only a small subinterval of values of a. This adjusting of a is particularly needed in computing the

https://doi.org/10.1017/S0956792504005741 Published online by Cambridge University Press

stable manifold of B when h_b is very small, since then the system is very sensitive to changes in h.

2.5 Parameter ranges for equilibria

For both the precursor and Navier slip models, we consider parameter values for which there are three equilibria. This places restrictions on the parameters, which we describe in two lemmas. In the *Navier Slip model*, there is a limited range of β for which there are three equilibria. Recall that equilibria $(\bar{h}, 0, 0)$ occur at intersections between the flux function, $f(h)$ and the line with slope $s = f(h_m)/h_m$ through the origin. The limits of the parameters will occur when the chord is tangent to the flux function, i.e.

$$f(h) = f'(h)h.$$

From $f(h) = h^2 - h^3 + \frac{2}{3}\beta - \beta h$, this equation becomes

$$h^3 - \frac{1}{2}h^2 + \frac{1}{3}\beta = 0. \tag{2.10}$$

The three roots have product $\frac{-\beta}{3} < 0$, so that when they are all real, two are positive and one is negative. The two positive roots coalesce when the minimum of the cubic (at $h = \frac{1}{3}$) is a root; this occurs precisely when $\beta = \frac{1}{18}$ (from setting $h = \frac{1}{3}$ in (2.10)). There is also a maximum at $h = 0$, at which the negative root coincides with a positive root, for $\beta = 0$. Thus, the range for β is

$$0 < \beta < \frac{1}{18}.$$

Now let $h_{min}(\beta) < h_{max}(\beta)$ be positive roots of equation (2.10). Then h_m is constrained by

$$h_{min}(\beta) < h_m < h_{max}(\beta). \tag{2.11}$$

We summarize the result as a lemma.

Lemma 2.1 *Let $h_{min}(\beta) < h_{max}(\beta)$ be positive roots of* (2.10). *Then there are three equilibria $0 < h_b < h_m < h_t$ for the Navier slip model* (2.4) *if and only if $0 < \beta < \frac{1}{18}$; consequently, $h_{min}(\beta) < h_m < h_{max}(\beta)$.*

Finally, note that for the Navier slip model, the wave speed s depends only on h_m: $s = \frac{f(h_m)}{h_m}$.

For the *precursor model* ($\beta = 0$), the precursor height h_b is constrained by $0 < h_b < \frac{1}{3}$. Here, we want three roots of the equation

$$f(h) - f(h_b) = s(h - h_b), \tag{2.12}$$

but we also want h_b to be the smallest root. Limits on s occur when s is the slope of the tangent to the graph of s at an equilibrium, either at h_b (for the minimum value of s) or at a larger equilibrium. Thus $s_{min} = f'(h_b) = 2h_b - 3h_b^2$, and $s = s_{max}$ is given by (2.12), together with

$$s = f'(h) = 2h - 3h^2. \tag{2.13}$$

https://doi.org/10.1017/S0956792504005741 Published online by Cambridge University Press

Equation (2.12) becomes, after dividing by $h - h_b \neq 0$,

$$s = -\left(h^2 + hh_b + h_b^2\right) + h + h_b. \tag{2.14}$$

Solving (2.13), (2.14), we find $s = s_{min}$ and $h = h_b$, or $s = s_{max} = \frac{1}{4} + \frac{1}{2}h_b - \frac{3}{4}h_b^2$ and $h = 1/2(1 - h_b)$. Thus the constraints on s and h_m are specified in the following lemma.

Lemma 2.2 *For the precursor model ((2.5) with $\beta = 0$), there are three equilibria $0 < h_b < h_m < h_t$ if and only if $2h_b - 3h_b^2 < s < \frac{1}{4} + \frac{1}{2}h_b - \frac{3}{4}h_b^2$, $h_b < h_m < 1/2(1 - h_b)$, and $0 < h_b < \frac{1}{3}$.*

Remark

For the Navier slip model, we trace trajectories in $W^U(M)$, and measure the most negative slope of those that go to $h = 0$ at a finite value of ξ. As we will see in the following section, these trajectories require that $W^U(M)$ and $W^S(B)$ intersect. As h_m is increased, these manifolds eventually separate at $h_m = h^*(\beta) < h_{max}(\beta)$.[1] Thus, we find trajectories for h_m in a range even more restricted than calculated in (2.11):

$$h_{min}(\beta) < h_m < h^*(\beta). \tag{2.15}$$

In the precursor model, we want trajectories that lie in both $W^U(M)$ and $W^S(B)$, i.e. trajectories (in $W^U(M) \cap W^S(B)$) that are heteroclinic orbits from M to B. Again, the parameter ranges are more limited than those of Lemma 2.2 due to the eventual separation of $W^U(M)$ and $W^S(B)$.

3 Numerical experiments

The overall goal of the numerical experiments is to determine the effective contact slope for each of the two models, and to determine the effect of varying parameters such as h_b, h_m and β. The effective contact slope is measured as the most negative value of h' for a single trajectory.

To compute trajectories, we used the implicit Adams method in LSODE, the Livermore Stiff ODE solver [21]. This solver is implemented with variable step size and variable order (first to twelfth).

Initial conditions (2.9) are numbered by an index j: $a = j * \delta$ and $j_{start} \leqslant j \leqslant j_{start} e^{\frac{2\pi\alpha}{\gamma}}$, in which δ is the spacing between initial points, numbered by j. The two parameters δ and j_{start} are used to refine calculations where needed. The two-dimensional manifolds $W^U(M), W^S(B)$ are visualized by computing their intersections with a Poincaré section, $h = (2h_m + h_b)/3$ (as in Bertozzi *et al.* [3]), so that each manifold is represented by a curve. To calculate Poincaré sections, we use $1000 \leqslant j \leqslant 37623$, and $\delta = 10^{-10}$. When refinement is needed in this process we take $\delta = 10^{-11}$. Note that to calculate $W^S(B)$ we integrate backwards in ξ.

Parameter choices for comparison of the two models, extending the range in Buckingham *et al.* [6], are shown in Table 2. The remaining parameter, namely the wave speed s, is calculated according to the formulae in Table 1. The values of h_b in

[1] The function $h^*(\beta)$ has to be calculated numerically.

https://doi.org/10.1017/S0956792504005741 Published online by Cambridge University Press

Table 2. *Parameter specifications*

h_m	0.26, 0.28, 0.30, 0.32
Navier slip model: β	0.007, 0.01, 0.013
Precursor model ($\beta = 0$): h_b	0.03, 0.033, 0.035, 0.04, 0.045, 0.05, 0.055, 0.06

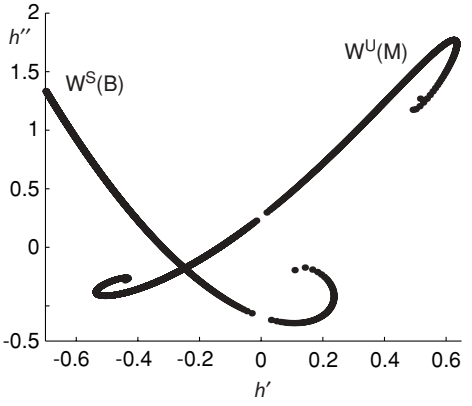

FIGURE 3. Macroscopic View of Poincaré section. $\beta = 0.013, h_m = 0.26$.

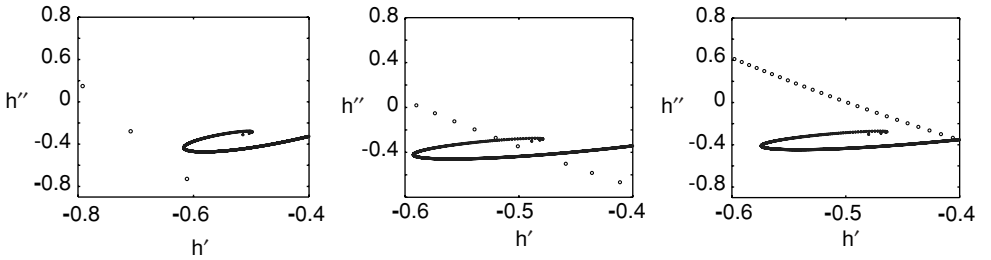

FIGURE 4. Poincaré sections for the precursor model: $h_b = 0.01, 0.023, 0.033; h_m = 0.26$.

the precursor model are chosen to be small enough to be in a realistic range; although smaller values would be desirable, simulations become unreliable at very small values of h.

3.1 Phase portraits and the Poincaré section

Since the ODEs for the two models have a similar structure, it is not surprising that their phase portraits are qualitatively similar. In Figure 3, we show a Poincaré section for the Navier slip model on a scale that illustrates the general structure of the manifolds $W^U(M), W^S(B)$. (The gaps around $h' = 0$ correspond to the manifolds becoming tangent to the plane $h = constant$; they can be made smaller by refining the initial data.) In Figure 4, we show intersections in the Poincaré section between $W^U(M)$ and $W^S(B)$ on a larger scale, as h_b varies from 0.01 to 0.033 in the precursor model. As h_b increases, we observe the line of dots representing trajectories in $W^S(B)$ pull through the spiral of

https://doi.org/10.1017/S0956792504005741 Published online by Cambridge University Press

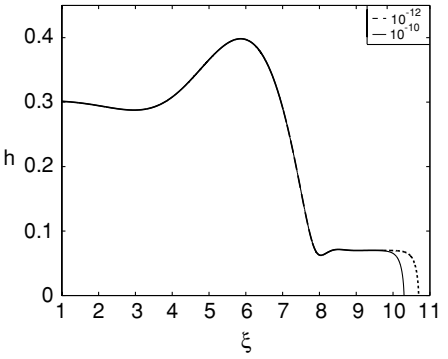

FIGURE 5. Effect of δ on precursor length. $h_b = 0.07$.

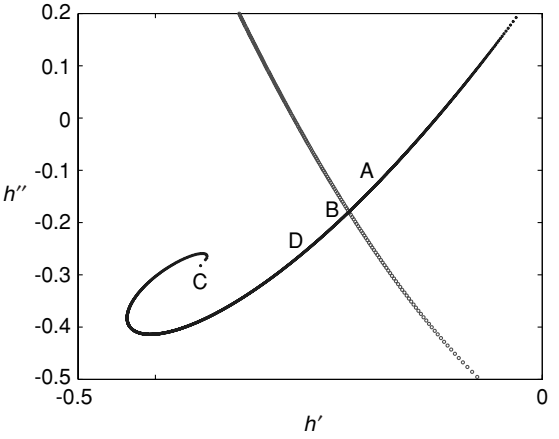

FIGURE 6. Single trajectories labeled on the Poincaré section. $\beta = 0.013, h_m = 0.26$.

$W^U(M)$, with varying numbers of intersections. Note that the smaller values of h_b fall outside the range for comparison of the two models given in Table 2. Specifically, for $h_b = 0.01$, there are no trajectories from M to B so we cannot calculate contact slopes for comparison with the Navier slip model. The values of h_m and h_b in Figure 4 were chosen to clarify the behavior of the Poincaré sections.

For the precursor model, intersections of the manifolds correspond to the relevant trajectories; they are heteroclinic orbits from M to B. A typical profile for such a trajectory is shown in Figure 5. (In this figure, we show only the portion near the contact line; for smaller ξ, the profile simply approaches the upstream height.) In the analytic solution, the precursor has infinite length. This could be achieved numerically by integrating backwards from B and forwards from M. To generate the figure, we chose two points on $W^U(M)$ close to $W^S(B)$, and superimposed the profiles to show how the precursor length increases slowly as the points are chosen closer to the intersection.

For the Navier slip model however, we seek trajectories from M to $h = 0$. We say such trajectories touch down. They are represented in the Poincaré section by portions of $W^U(M)$ to the left of $W^S(B)$ in Figure 6. In Figure 7 we show individual trajectories (again focussing in on variations in the film shape near the contact line) for points

https://doi.org/10.1017/S0956792504005741 Published online by Cambridge University Press

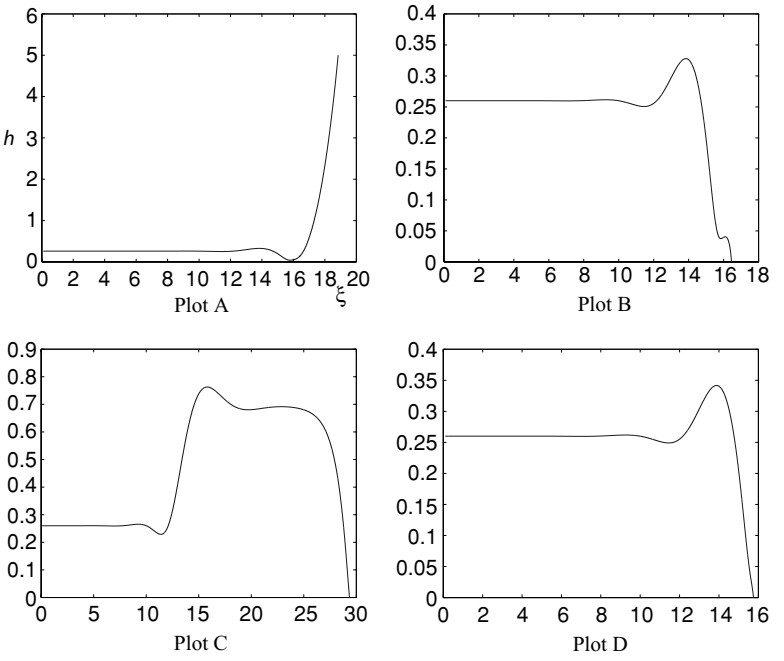

FIGURE 7. Navier slip model: single trajectories. $\beta = 0.013, h_m = 0.26$.

A,B,C, and D shown on $W^U(M)$ in Figure 6 to illustrate a variety of profile shapes. In Figure 7A, the trajectory corresponds to a point in $W^U(M)$ on the wrong side of $W^S(B)$; consequently, $h \to \infty$. The three trajectories in Figure 7 B,C,D are taken from points around the arc of $W^U(M)$ on the side of $W^S(B)$ corresponding to trajectories that touch down. The profile in Figure 7B shows a small oscillation as h approaches zero. In the three-dimensional phase portrait, the corresponding trajectory approaches the equilibrium at B, and undergoes a rotation about the one-dimensional unstable manifold from B. Note that the point labeled B in Figure 7 is close to $W^S(B)$. The profile in Figure 7C does not have this oscillation near $h = h_b$, but instead has a plateau around $h = h_t$. In the phase portrait, the corresponding trajectory approaches the equilibrium at T, and has a small rotation around the one-dimensional unstable manifold from T before decreasing monotonically to $h = 0$. Between these two extremes, we show a trajectory in 7D that has neither of the features of Figures B and C. In Figures B and D, there is a well-defined capillary ridge[2] where h reaches its maximum. In Figure C, there is a much broader and taller capillary ridge.

3.2 Contact slopes

We wish to compare the two models by investigating how well they represent the contact angle, the angle the fluid surface makes with the solid surface at the contact line. Both models present difficulties in this regard. The precursor model is formulated specifically

[2] The capillary ridge is a commonly observed feature in experiments on driven thin liquid films (cf. Cazabat *et al.* [7]).

https://doi.org/10.1017/S0956792504005741 Published online by Cambridge University Press

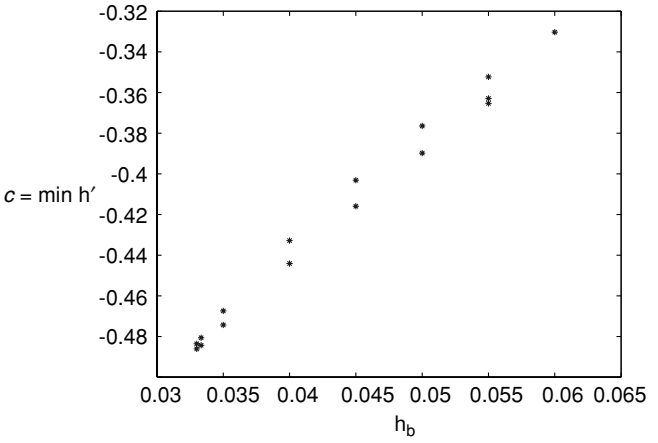

FIGURE 8. Effective contact slope c vs. h_b. Precursor model, $h_m = 0.30$.

to avoid having a contact line. In this case, the contact angle should be what is observed experimentally, assuming a small precursor height. By considering only traveling waves, we are not able to consider arbitrarily small precursor layers, as explained above. Moreover, the observed contact angle, associated with the steepest slope of the profile, depends on the precursor height, as shown in Figure 8. In this figure, we show the steepest slope for all trajectories (up to three for the level of accuracy of the calculations) corresponding to intersections of $W^U(M)$ with $W^S(B)$, for a range of precursor heights h_b. Observe that the (negative) slopes fall into an interval that is bounded below[3]. The lower bound is achieved at a value of h_b for which $W^U(M)$ and $W^S(B)$ have tangential intersection; for smaller values of h_b, these manifolds do not intersect. This signals the splitting of a wave into a two-wave solution of the PDE. In § 4, we relate this transition to the nucleation condition formulated in LeFloch and Shearer [15].

For the Navier slip model, there is a contact line, where $h = 0$. However, as illustrated in Figure 7B, it may not be appropriate to measure the slope h' precisely at this point. The *effective contact slope* is the most negative slope beyond the capillary ridge. For this model, for each choice of $\beta > 0$, there are infinitely many trajectories, each with its own effective contact slope c. The slopes as a function of location on $W^U(M)$, indexed by j, are shown in Figure 9 for $\beta = 0.013$. As for the precursor model, the contact slopes fall into an interval, but in this case the interval has well-defined upper and lower bounds. In Figure 10, we plot effective contact slope against $h'(0)$. It is striking how different this plot is from the corresponding monotonic curves of Tuck & Schwartz [20], in the absence of Marangoni force, where $h'(0)$ approaches zero at one end, and is apparently unbounded at the other end. Moreover, the effective contact slope and $h'(0)$ approach each other in Tuck & Schwartz [20], whereas here there is apparently no range in which the two measures of contact slope agree.

We first compare the models by comparing the ranges (i.e. intervals) of these slopes, rather than the individual values. In Figure 11, the intervals are represented by symbols

[3] The interval is also bounded above (by zero), but slopes closer to zero than those shown in Figure 8 are achieved only by taking physically unrealistic precursor heights.

https://doi.org/10.1017/S0956792504005741 Published online by Cambridge University Press

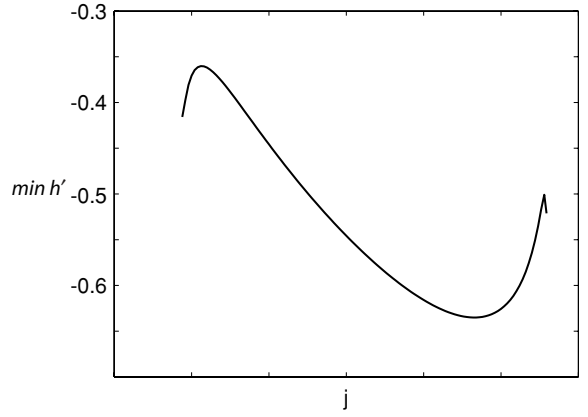

FIGURE 9. Contact slopes for Navier Slip, $\beta = 0.013, h_m = 0.26$.

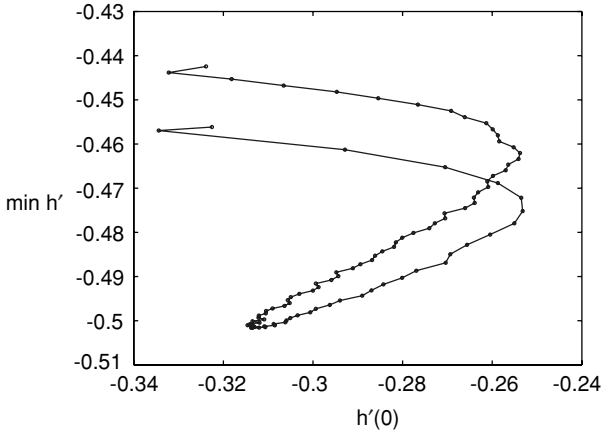

FIGURE 10. Effective contact slope vs. actual contact slope. Navier Slip, $\beta = 0.007, h_m = 0.26$.

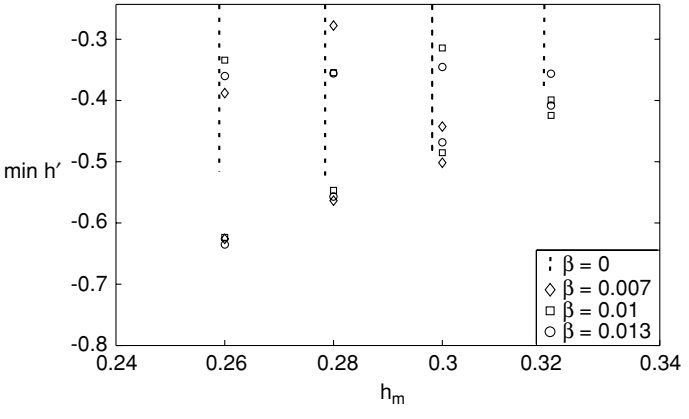

FIGURE 11. Ranges of contact slope, $\beta \geqslant 0$.

https://doi.org/10.1017/S0956792504005741 Published online by Cambridge University Press

showing their upper and lower limits, for a variety of values of upstream height h_m and slip parameter $\beta > 0$. We also indicate, with a dashed line, the range of contact slopes for the precursor model ($\beta = 0$). The range of contact slopes c (a typical plot is Figure 9) was calculated for each choice of model parameters with $\delta = 10^{-10}$. To check the accuracy of the upper and lower limits of this range recorded in Figure 11, refinement using $\delta = 10^{-11}$ was performed near these limits. The conclusion of this refinement is that the limiting values of c are accurate to four decimal places for both models. Note that on the right hand side of the figure, we lose a data point in the Navier slip model for $h_m = 0.32$ and $\beta = 0.007$ since $W^S(B)$ and $W^U(M)$ do not intersect, even though (2.11) holds.

If we consider only the most negative slopes in the Navier slip model, they are relatively independent of β, and monotonically increasing with h_m. For the precursor model, the most negative slopes are generally smaller (less negative) than those of the Navier slip model, and they are not monotonic in h_m. On the other hand, if we consider the least negative slopes (represented by the upper symbols in Figure 11), those for the Navier slip model are not monotonic, but are decreasing for larger h_m. The least negative slopes for the precursor model are comparable to those of the Navier slip model; however they are achieved at larger h_b (see Figure 8).

To further compare the two models, we need to identify specific points in the intervals shown in Figure 11. To do so, we compare contact slopes for like profiles, meaning those with the same global maximum of h, as in Tuck & Schwartz [20]. First, we fix a specific profile $h_0(\xi)$ for the precursor model, with chosen upstream and precursor heights h_m and h_b, respectively. For fixed $\beta \neq 0$ (the Navier slip model), there is a one-parameter family of profiles with the same upstream height, and we select the profile that matches the maximum height $\max_\xi h_0(\xi)$ of the precursor profile. We can then compare maximum slopes for the two profiles. As pointed out in Tuck & Schwartz [20], this procedure requires careful selection of β. Below a minimum β, all profiles have maximum height greater than that of h_0. Accordingly, we select $h_0(\xi)$ using Figures 8 and 11 as follows, in order to get a reasonable range for β. From Figure 11 we observe that $h_m = 0.28$ and $h_m = 0.3$ both have all four contact slope intervals overlapping; we choose $h_m = 0.3$ in order to provide a bigger challenge for the comparison – the interval of overlap is quite small. To provide a precursor profile for comparison, we choose a value $\min h' = -0.47$ in the center of this interval of overlap, and then find the corresponding value $h_b = 0.037$ of the precursor height (from Figure 8) at which the maximum slope is approximately this value. For $h_m = 0.3, h_b = 0.037$ and $\beta = 0$ we found two intersections between $W^U(M)$ and $W^S(B)$, and a single trajectory corresponding to each intersection. We calculated the global maximum for each of the two trajectories and then sought corresponding trajectories with matching global maximum, for the same fixed $h_m = 0.3$, and the varying $\beta = 0.007, 0.01, 0.013$. Figure 12 shows these plots superimposed. Note that there is some variation in the maximum slope as β varies, but that this variation is very small. The difference between the contact slope for the $\beta = 0$ case (for either intersection) differs from the maximum contact slope for the $\beta \neq 0$ cases from approximately 1–6% of the contact slope for the $\beta = 0$ case. At a macroscopic level, there is very good agreement between the profiles. The lateral separation of the trajectories is less than one percent of the distance between the global minimum and maximum of the trajectories. Zooming in

https://doi.org/10.1017/S0956792504005741 Published online by Cambridge University Press

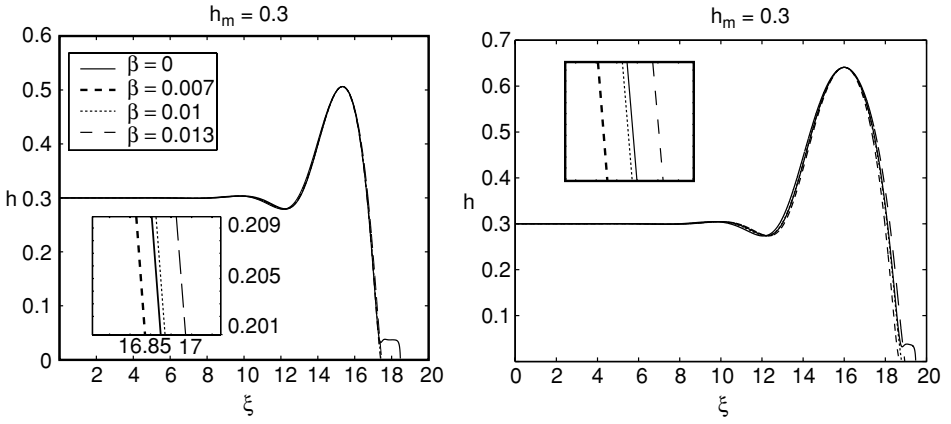

FIGURE 12. Comparison of profiles for two intersections of $W^U(M), W^S(B)$, $h_b = 0.037$.

on these differences in Figure 12, we can again see good agreement, and observe that the difference is not monotonic in β, suggesting that the contact slopes may not be as well.

4 The kinetic relation and nucleation condition

In this section, we describe another use of the calculation of invariant manifolds of the third order ODE in the precursor model. Some of the phenomena observed in experiments and in simulations of the PDE (1.1) can be explained from a theory of hyperbolic wave solutions of the underlying scalar conservation law, as explained in LeFloch & Shearer [15]. This theory encapsulates information from the traveling wave problem in two functions of the precursor height, namely the *kinetic function* which we label $h_K(h_b)$, and the *nucleation function* $h_N(h_b)$. The kinetic function[4] specifies the value $h_t = h_K(h_b)$ for which there is an undercompressive shock joining the upstream height h_t to the precursor with height h_b. The nucleation function plays the role of determining the value of upstream height at which undercompressive waves are forced to appear, i.e. nucleate.

These two functions are left unspecified in the general hyperbolic theory of LeFloch & Shearer [15]). Here, we capture graphs of the two functions by considering traveling wave solutions of (1.1). For a given $h_b < 1/3$, we find the value $h_t = h_K(h_b)$ for which there is an undercompressive traveling wave, i.e. an orbit joining the equilibrium T to the equilibrium B. This occurs when the unstable manifold from T lies on the stable manifold of B, a criterion we can easily determine in the Poincaré section by finding the value of the upstream height h_m for which $W^U(B)$ intersects the spiral-shaped $W^U(M)$ through its center (see Figure 13A). Similarly, as the manifold $W^U(M)$ detaches from the manifold $W^S(B)$, corresponding to the smallest value of h_m for which there are no orbits from M to B, we conclude that the PDE must revert to a two-wave structure, thereby nucleating an undercompressive wave. The nucleation function is then the value $h_m = h_N(h_b)$ at which this occurs (see Figure 13B).

[4] The kinetic function is the subject of an extensive theory of nonclassical weak solutions of scalar conservation laws and systems [14].

https://doi.org/10.1017/S0956792504005741 Published online by Cambridge University Press

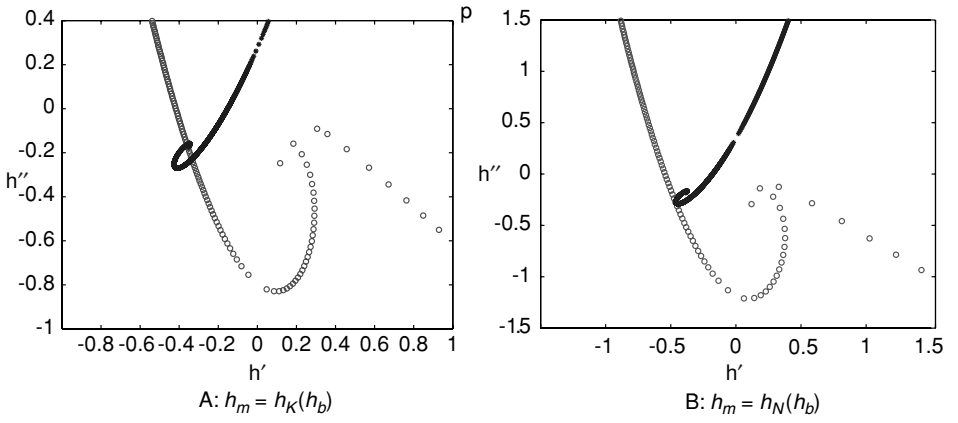

FIGURE 13. Poincaré Sections for A: Kinetic relation; B: Nucleation condition.

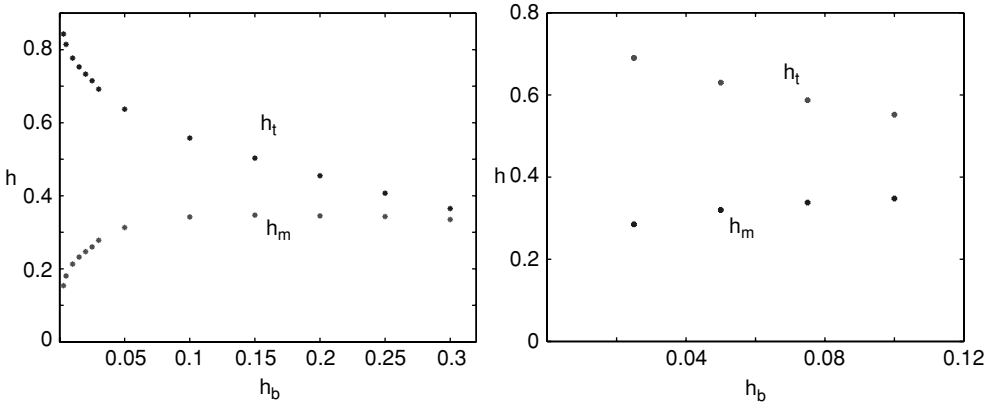

FIGURE 14. Kinetic relation (left) and Nucleation condition (right).

In Figure 14, we show the results of these calculations for a range of values of h_b. In the figure, we plot numerical data for both the middle and top equilibria for the kinetic relation and the nucleation condition.

5 Discussion

In this paper, we have explored the possibilities of comparing different slip models for moving contact lines by analyzing traveling waves, in the very specific context of a thin film driven up an inclined plane by a Marangoni force, against the action of gravity. This setting gives rise to behavior of the contact line rather different from other cases in which there is a single force, as noted in the earlier paper [6]. In the current paper, we have compared the singular slip model with a range of parameters to the precursor model, with a range of precursor thicknesses.

The techniques of this paper are comparable to those of the earlier studies [20] (in which both precursor and Navier slip models were considered for gravity-driven films), and of Buckingham *et al.* [6] (which is concerned solely with novel features of the Navier slip

https://doi.org/10.1017/S0956792504005741 Published online by Cambridge University Press

model with both gravity and Marangoni force). We find that the range of effective contact slopes in both models is confined to an interval bounded away from zero. Moreover, the precursor model breaks down in an unexpected way as the precursor height is decreased for a given upstream height: below a critical precursor height, there are no traveling waves from the upstream height to the precursor, even when both heights are equilibria of the ODE. This is explained with the aid of Poincaré sections of the phase diagram of the ODE.

It would be interesting to investigate the stability of the traveling waves. There are some results for the precursor model [4], but for the Navier slip model, stability is harder to formulate, as the traveling wave does not extend over the entire real line; it's stability would depend on setting a boundary condition at the contact line.

In agreement with the gravity driven case [20], we find excellent correspondence between effective contact slopes for profiles with the same maximum height. However, such a comparison severely limits the range of parameters, as a precursor model profile may have no comparable profile for the slip model. A second, more understandable limitation is that not all solutions of initial value problems converge to traveling waves. Indeed, simulations of the thin film PDE [3] show clearly that for some choices of upstream and precursor height, there is no traveling wave, and PDE solutions are forced to converge to a solution that has two-wave structure. In this vein, it is possible to understand the two-wave structure, and the disappearance of the traveling waves, through a careful analysis of the traveling wave equation, leading to an example of kinetic relation and nucleation condition. These encapsulate information about the surface-tension-driven flow that can be used in the hyperbolic conservation law representing the limit of vanishing surface tension. This issue is explored in more detail in the forthcoming paper [16].

Acknowledgements

The research for this article was supported by NSF Grants DMS-9803305, DMS-0244491. The authors gratefully acknowledge the support and assistance provided by the Isaac Newton Institute for Mathematical Sciences, Cambridge and the North Carolina Supercomputing Center. We also gratefully acknowledge valuable discussions with Robbie Buckingham, Andrea Bertozzi, Jeanman Sur, together with technical assistance from Randall Nortman. Michael Shearer is an Adjunct Professor in the Department of Mathematics at Duke University.

References

[1] Bertozzi, A. L. & Bowen, M. (2002) Thin films and moving contact lines. In: Bourlioux, A., Gander, M. J. and Sabidussi, G. (eds.), *Modern Methods in Scientific Computing and Applications, Proceedings of the Nato Adv. Study Institute*. Nato Science Series II, Vol. 75, Kluwer, Dordrecht, pp. 31–79.

[2] Bertozzi, A. L. (1998) The mathematics of moving contact lines in thin liquid films. *Notices Am. Math. Soc.* **45**, 689–697.

[3] Bertozzi, A. L., Münch, A. & Shearer, M. (1999) Undercompressive shocks in thin film flows. Physica D, **134**, 431–464.

[4] Bertozzi, A. L., Münch, A., Shearer, M. & Zumbrun, K. (2000) Stability of compressive and undercompressive thin film travelling waves. *Euro. J. Appl. Math.* **12**, 253–291.

[5] Bertozzi, A. L. & Shearer, M. (2000) Existence of undercompressive traveling waves in thin film equations. *SIAM J. Math. Anal.* **32**, 194–213.
[6] Buckingham, R., Shearer, M. & Bertozzi, A. L. (2003) Thin film traveling waves and the Navier slip condition. *SIAM J. Appl. Math.* **63**, 722–744.
[7] Cazabat, A. M., Heslot, F., Troian, S. M. & Carles, P. (1990) Finger Instability of Thin Spreading Films driven by temperature gradients. *Nature*, **346**, 824–826.
[8] Dussan, E. B. & Davis, S. (1974) On the motion of a fluid-fluid interface along a solid surface. *J. Fluid Mech.* **65**, 71–95.
[9] de Gennes, P. G. (1985) Wetting: Statics and dynamics. *Rev. Mod. Phys.* **57**, 827.
[10] Goldstein, S. (1965) *Modern Developments in Fluid Mechanics, vol. 2.* Dover.
[11] Greenspan, H. P. (1978) On the motion of a small viscous droplet that wets a surface. *J. Fluid Mech.* **84**, 125–143.
[12] Hocking, L. M. (1977) A moving fluid interface. Part 2: The removal of the force singularity by a slip flow. *J. Fluid Mech.* **79**, 209–229.
[13] Huh, C. & Scriven, L. E. (1971) Hydrodynamic model of steady movement of a solid/liquid/fluid contact line. *J. Coll. Int. Sci.* **35**, 85–101.
[14] LeFloch, P. G. (2002) Hyperbolic systems of conservation laws: The theory of classical and nonclassical shock waves. *Lectures in Mathematics*, ETH Zürich, Birkhäuser.
[15] LeFloch, P. G. & Shearer, M. (2004) Nonclassical Riemann solvers with nucleation. *Proc. A Roy. Soc. Edinburgh* **134A**, 961–984.
[16] Levy, R. & Shearer, M. (1971) Kinetics and nucleation for driven thin film flow. *Physica D* (to appear).
[17] Ludviksson, V. & Lightfoot, E. N. (1971) The dynamics of thin liquid films in the presence of surface-tension gradients. *Am. Inst. Chem. Eng. J.* **17**, 1166–1173.
[18] Münch, A. (2000) Shock transitions in Marangoni-gravity driven thin film flow. *Nonlinearity*, **13**, 731–746.
[19] Navier, C. (1823) Memoire sur les lois du mouvement des fluids. *Memoires de l'Academie Royale des Sciences de l'Institut de France*, **6**, 389–440.
[20] Tuck, E. O. & Schwartz, L. W. (1990) A numerical and asymptotic study of some third-order ordinary differential equations relevant to draining and coating flows. *SIAM Rev.* **32**, 453–469.
[21] Radhakrishnan, K. & Hindmarsh, A. (1994) Description and use of LSODE. NASA ref. pub. 1327, LLNL Report UCRL-1D-113855. (http://www.llnl.gov/CASC/nsde/pubs/u113855.pdf)
[22] Sur, J., Bertozzi, A. L. & Behringer, R. P. (2003) Reverse undercompressive shock structures in driven thin film flow. *Phys. Rev. Lett.* **90**, 126105.
[23] Witelski, T. P., Bernoff, A. J. & Bertozzi, A. L. (2004) Blow-up and dissipation in a critical-case unstable thin film equation. *Euro. J. Appl. Math.* **15**, 223–256.